Hybrid model calculations of direct photons in high-energy nuclear collisions

Bjørn Bäuchle[1,2,*] and Marcus Bleicher[2]
[1]*Frankfurt Institute for Advanced Studies, D-60438 Frankfurt am Main, Germany*
[2]*Institut für Theoretische Physik, Goethe-Universität, D-60438 Frankfurt am Main, Germany*
(Received 7 August 2009; revised manuscript received 4 March 2010; published 13 April 2010)

Direct photon emission in heavy-ion collisions is calculated within a relativistic micro + macro hybrid model and compared to the microscopic transport model, the Ultra-relativistic Quantum Molecular Dynamics model. In the hybrid approach, the high-density part of the evolution is replaced by an ideal three-dimensional hydrodynamic calculation. This allows the effects of viscosity and full local thermalization, in comparison with the transport model of the ideal fluid dynamics, to be examined. The origin of high-$p_\perp$ photons as well as the impact of elementary high-$\sqrt{s}$ collisions is studied. The contribution of different production channels and nonthermal radiation to the spectrum of direct photons is further explored. Detailed comparisons to the measurements by the WA98 Collaboration are also undertaken.

DOI: 10.1103/PhysRevC.81.044904 PACS number(s): 25.75.Cj

I. INTRODUCTION

Creating and studying high-density and high-temperature nuclear matter is the major goal of heavy-ion experiments. A state of quasifree partonic degrees of freedom, the quark-gluon plasma (QGP) [1,2], may be formed if the energy density in the reaction is high enough. Strong jet quenching, large elliptic flow, and other observations made at the BNL Relativistic Heavy Ion Collider (RHIC) suggest the successful creation of a strongly coupled QGP at these energies [3–6]. Possible evidence for the creation of this new state of matter was also put forward by collaborations at the CERN Super Proton Synchrotron (SPS): for instance, the step in the mean transverse mass excitation function of protons, kaons, and pions and the enhanced K^+/π^+ ratio [7].

Out of the many possible observables, electromagnetic probes have the advantage of leaving the hot and dense region undisturbed: once they are created, they escape freely from the reaction zone because of their negligible rescattering cross sections. Besides dileptons, direct photon emission is of greatest interest to gain insight into the early, hot, and therefore possibly partonic stages of the reaction. Direct photons are distinguished from the bulk of photons as those coming from collisions and not decays.

Unfortunately, the overwhelming amount of photons in heavy-ion collisions comes from hadronic decays in the late stages, mostly $\pi^0 \to \gamma\gamma$. These decay photons impose a serious challenge for the experimental extraction of direct photon data. Until now, several experiments went through the challenge of obtaining the spectra of direct photons: the Helios Collaboration, the WA80 Collaboration, and the CERES Collaboration (all at the CERN SPS) could publish upper limits, whereas the WA98 Collaboration (CERN-SPS) [8] and the PHENIX Collaboration (BNL RHIC) [9,10] published explicit data points for direct photons.

On the theoretical side, calculations for the elementary photon production processes have been known for a long time (see, e.g., Kapusta *et al.* [11] and Xiong *et al.* [12]). The major problem here is the difficulty of describing the time evolution of the produced matter, which, until now, was not possible from first-principle quantum chromodynamics (QCD). One has to rely on well-developed dynamical models to describe the space-time evolution of nuclear interactions in the hot and dense stage of the reaction. A well-established approach to explore the dynamics of heavy-ion reactions is relativistic transport theory [13–21]. In this kind of microscopic description, the hadronic and/or partonic stage of the collision is described under certain approximations. Most transport models, for instance, cannot describe collisions with more than two incoming particles, which restricts the model applicability to low particle densities, where multiparticle interactions are less important. Some attempts to include multiparticle interactions do exist [18,22–26], but this field of study is still rather new. The coupling of a partonic phase with a hadronic phase poses another challenge in transport models, because the microscopic details of that transition are not well known. Another complication in the transport approach is that all microscopic scatterings are explicitly treated in the model and therefore the cross sections for all processes must be known or extrapolated. However, for many processes, high-quality experimental data are not available, and therefore a large fraction of the cross sections have to be calculated or parametrized by additional models.

Relativistic, (non)viscous fluid or hydrodynamics involves a different approach to explore the space-time evolution of a heavy-ion collision [27–42]. It constitutes a macroscopic description of the matter that is created, assuming that at every time and in every place the matter is in local thermal equilibrium. This assumption can only be true if the matter is sufficiently dense; in the late stages of a heavy-ion collision, fluid dynamics loses applicability. In addition, the requirement of local thermal equilibrium restricts the starting time of the hydrodynamic model. An advantage is that, in the dense stages, hydrodynamics can propagate any kind of matter and also allows for transitions between two types of matter (e.g., QGP and hadron gas) if an appropriate equation of state (EOS)

*baeuchle@th.physik.uni-frankfurt.de

is provided. Fluid dynamics can therefore be used to study hadronic and partonic matter in one common framework.

The restrictions of these kinds of models can be relaxed as well. By introducing viscosity and heat conductivity, perfect thermal equilibrium does not have to be present at any point. However, even with second-order corrections, the matter has to be close to equilibrium [43–45].

Input to solve the hydrodynamic differential equations are the boundaries (i.e., the initial state—the distributions of all relevant densities and currents at the time the evolution starts), the EOS providing the pressure as a function of the energy and baryon densities, which describes the behavior of the matter that is considered, and the freeze-out hypersurface.

Finally, approaches to the theoretical description of direct photon spectra may include calculations in perturbative QCD (pQCD). Calculations based on pQCD describe the high-$p_\perp$ photon data in proton-proton collisions very well and, if scaled by the number of binary nucleon-nucleon collisions, also those in heavy-ion reactions. However, the range of applicability of these calculations is limited to high transverse momenta $p_\perp^\gamma \gg 1$ GeV.

The different approaches have different limits of applicability. For example, thermal rates can only be applied if the assumption of local thermal equilibrium is fulfilled. Photon emission rates can then be calculated by folding the particle distribution functions of the participating particle species with the respective cross sections. This framework can be applied to static models, simplified hydrodynamics-inspired models such as the blast wave model, and to full fluid-dynamical calculations. The space-time evolution of a reaction as predicted by microscopic theories can be averaged over to apply thermal rates to the coarse-grained distributions [39]. The application of microscopic cross sections can only be undertaken in a model where all microscopic collisions are known, which limits the field of use to transport models. For previous calculations of photon spectra from transport models see, for example, Refs. [46–48].

In this article, we investigate the spectra of direct photons coming from microscopic hadronic scatterings, thermal hadronic and partonic emissions, and hard initial pQCD scatterings. We compare results from a purely microscopic model to those from an integrated micro + macro hydrodynamic approach that embeds a hydrodynamic phase into the Ultra-relativistic Quantum Molecular Dynamics (UrQMD) approach. The paper is organized as follows. First, we explain the hybrid model (Sec. II). In Sec. III, we elaborate on the photon sources considered in the model. In Secs. IV, V, and VI, the model is applied to compare thermal rates from microscopic theory to those from the literature, to compare different physics assumptions with experimental data from the WA98 Collaboration [8], and to analyze the sources of photon emission.

II. THE HYBRID MODEL

A. Transport model

UrQMD version 2.3 is a microscopic transport model [14,15,49]. It includes all hadrons and resonances up to masses

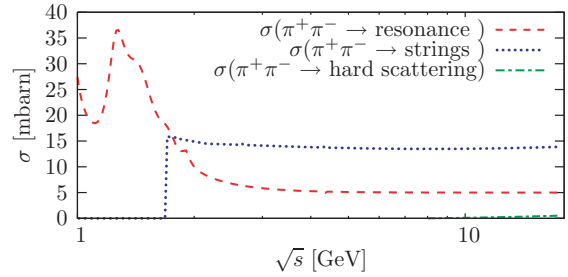

FIG. 1. (Color online) UrQMD cross sections for $\pi^+\pi^-$ collisions as a function of center-of-mass energy. The resonant hadronic cross section [(red) dashed line], the cross section for the formation of strings [(blue) dotted line], and the cross section for hard scatterings via PYTHIA [(green) dash-dotted line] are shown. The peak at the ρ-meson pole mass has been cut out for better visibility.

$m \approx 2.2$ GeV and at high energies can excite and fragment strings. The cross sections are parametrized, calculated via detailed balance, or taken from the additive quark model if no experimental values are available. At high parton momentum transfers, PYTHIA [50] is employed for pQCD scatterings.

UrQMD differentiates between two regimes for the excitation and fragmentation of strings. Below a momentum transfer of $Q < 1.5$ GeV, a maximum of two longitudinal strings are excited according to the Lund picture; at momentum transfers above $Q > 1.5$ GeV, hard interactions are modeled via PYTHIA. Figure 1 shows the total cross sections of resonant hadronic interactions, string excitation, and (hard) PYTHIA scatterings as a function of the center-of-mass energy of the collision, $\sqrt{s_{\text{coll}}}$. The contribution of hard scatterings to the total $\pi^+\pi^-$ cross section at the highest SPS energies ($\sqrt{s} \approx 17.3$ GeV) is about 4%. Figure 2 shows a comparison between charged-particle spectra from proton-proton collisions calculated in UrQMD with and without the PYTHIA contribution. For detailed information on the inclusion of PYTHIA, the reader is referred to Sec. II of Ref. [49].

In the UrQMD framework, all particle properties (mass, width, spectral shape) are taken at their vacuum values, and the propagation is performed without potentials (cascade mode). UrQMD was used earlier by Dumitru *et al.* to study direct photon emission [46]; a brief comparison between their results and the results obtained with this approach can be found in Appendix C.

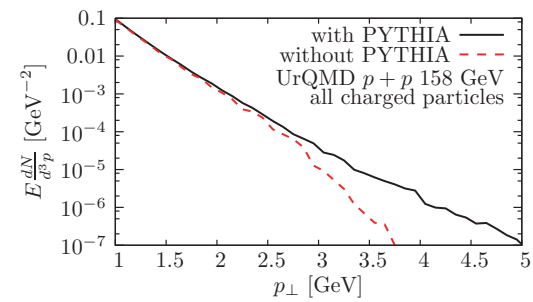

FIG. 2. (Color online) Charged-particle spectra from proton-proton collisions at $E_{\text{lab}} = 158$ GeV calculated with UrQMD with (solid black line) and without [dashed (red) line] PYTHIA.

B. Hybrid model

In the following, we compare results from this microscopic model to results obtained with a hybrid model description [51]. Here, the high-density part of the reaction is modeled using ideal $(3+1)$-dimensional fluid dynamics. The unequilibrated initial state and the low-density final state are described by UrQMD. Thus, those stages are mainly governed by string dynamics (initial state) and hadronic rescattering (final state).

To connect the initial transport phase to the fluid-dynamical phase, the baryon number density, energy density, and momentum density are smoothed and put into the hydrodynamic calculation after the incoming nuclei have passed through each other. Note that, in noncentral collisions, the spectators are propagated in the cascade. Thus, the initial state for the hydrodynamic stage is subject to both geometrical and event-by-event fluctuations. Temperature, chemical potential, pressure, and other macroscopic quantities are determined from the densities by the EOS used in the current calculation. During this transition, the system is forced into an equilibrated state, regardless of the actual level of equilibration before the transition. The initial temperature profile at $z = 0$ for a sample Pb + Pb event with $b = 0$ fm and $E_{\text{lab}} = 158A$ GeV for two different EOS (bag model and hadron gas) is shown in Fig. 3. Then the ideal $(3+1)$-dimensional hydrodynamic equations are solved on a grid using the SHASTA algorithm [36].

After the local rest frame energy density dropped below a threshold value of $\epsilon_{\text{crit}} = 730$ MeV/fm^3 ($\approx 5\epsilon_0$) with $\epsilon_0 \approx 146$ MeV/fm^3 being the nuclear ground-state energy density, particles are created on an isochronous hypersurface from the densities by means of the Cooper-Frye formula, and propagation is continued in UrQMD.

The transition scenario chosen for the present studies is always isochronous; that is, the whole system must meet the criterion at the same calculational time frame before the transition is performed. Earlier investigations within this hybrid model included an extensive analysis of the effect of changing the transition criterion [51], the strangeness production [52,53], the HBT correlations [54], the transverse mass [55], and the elliptic flow [56].

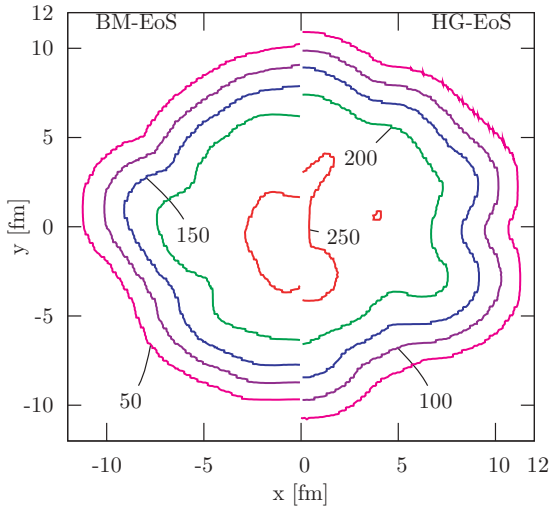

FIG. 3. (Color online) Temperature profiles after switching to fluid-dynamical description, calculated with the bag model (left) and hadron gas EOS (right). Along the lines, the temperature is constant, going from $T = 50$ MeV at the outermost line to $T = 250$ MeV at the innermost. Calculations have been done for Pb + Pb collisions at $E_{\text{lab}} = 158A$ GeV with $b = 0$ fm.

C. Equations of state

For the investigations presented here, different EOS are used for the hydrodynamic phase. The base line calculations are done with a hadron gas EOS (HG-EOS), which includes the same degrees of freedom that are present in the transport phase. This allows explore the effects due to the change of the dynamic description to be explored. Second, a MIT bag-model EOS (BM-EOS) with a partonic phase and a first-order phase transition [36] is employed. The BM-EOS thus allows for investigations of photon emission from the QGP. To obtain meaningful values of temperature and chemical potentials from the densities, the BM-EOS is smoothly transferred to the HG-EOS just above the transition energy density.

III. PHOTON EMISSION SOURCES

Photon emission is calculated perturbatively in both hydrodynamics and transport scenarios, because the evolution of the underlying event is not altered by the emission of photons due to their very small emission probability. The channels considered for photon emission may differ between the hybrid approach and the binary scattering model. Emission from a QGP can only happen in the hydrodynamic phase, and only if the EOS used has partonic degrees of freedom. Photons from baryonic interactions are neglected in the present calculation. The emission of hard photons from early pQCD scatterings of nucleons is calculated separately and incoherently added to the simulated spectra.

A. Photons from microscopic collisions

In the transport part of the (hybrid) model, each scattering is examined and the cross section for photon emission is calculated. Here, we employ the well-established cross sections from Kapusta *et al.* [11] and Xiong *et al.* [12]. Kapusta and collaborators based their calculations on the photon self-energy derived from a Lagrange density involving the pion, ρ, and photon fields

$$\mathcal{L} = |D_\mu \Phi|^2 - m_\pi^2 |\Phi|^2 - \tfrac{1}{4}\rho_{\mu\nu}\rho^{\mu\nu} + \tfrac{1}{2}m_\rho^2 \rho_\mu \rho^\mu - \tfrac{1}{4}F_{\mu\nu}F^{\mu\nu}, \tag{1}$$

where Φ is the pion field; $\rho_{\mu\nu} = \partial_\mu \rho_\nu - \partial_\nu \rho_\mu$ and $F_{\mu\nu} = \partial_\mu A_\nu - \partial_\nu A_\mu$ are the ρ and photon field strength tensors, respectively; and $D_\mu = \partial_\mu - \imath e A_\mu - \imath g_\rho \rho_\mu$ is the covariant derivative. The ρ-decay constant g_ρ is calculated from the total width Γ^ρ_{tot} of the ρ-meson:

$$g_\rho^2 = 48\pi \frac{\Gamma^\rho_{\text{tot}} m_\rho^2}{\left(\sqrt{m_\rho^2 - 4m_\pi^2}\right)^3}. \tag{2}$$

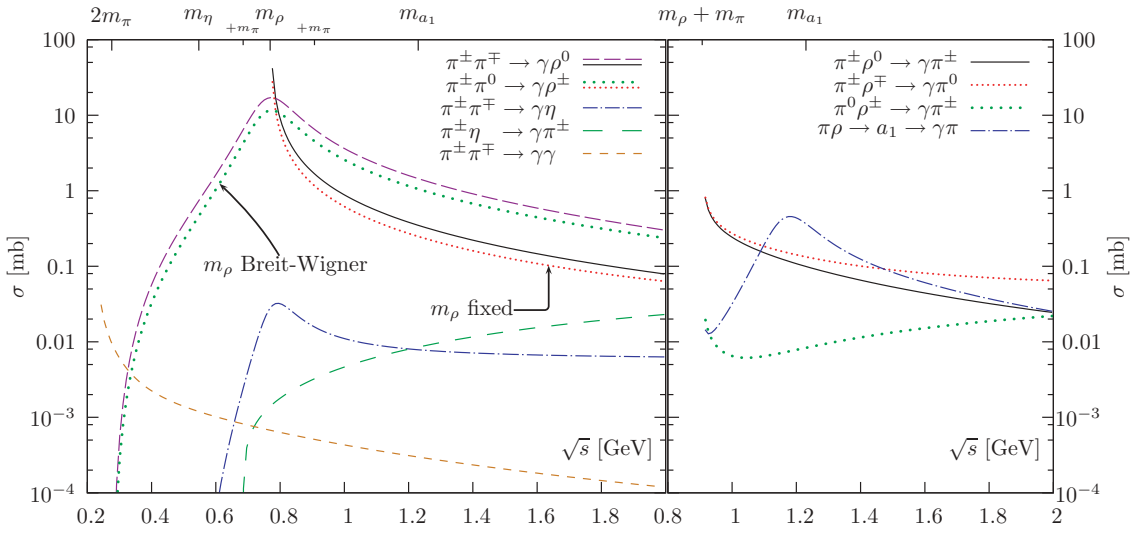

FIG. 4. (Color online) Cross sections for all included channels as a function of $\sqrt{s}$. For visibility, the cross sections for all processes $\pi\rho \to \gamma\pi$ are shown separately. They have been calculated with a ρ-mass $m_\rho = 0.769$ GeV. The left plot shows the cross sections for $\pi\pi \to \gamma\rho$ both for fixed ρ-mass ($m_\rho = 0.769$ GeV, labeled "m_ρ fixed") and for variable ρ-mass (labeled "m_ρ Breit-Wigner").

The differential cross sections used for the present investigation [11,12] are given in Appendix D.

All scatterings during the transport phase are examined to obtain direct photon spectra. For every scattering that may produce photons (i.e., those that have initial states equal to the processes listed in Appendix D), the corresponding fraction of a photon,

$$N_\gamma = \frac{\sigma_{\mathrm{em}}}{\sigma_{\mathrm{tot}}}, \tag{3}$$

is produced. Here, σ_{tot} is the sum of the total hadronic cross section for a collision with these ingoing particles (as provided by UrQMD) and the electromagnetic cross section σ_{em} as calculated by the aforementioned formulas. To obtain the correct angular distribution of the produced photons and to enhance statistics, for each scattering many fractional photons are created that populate all kinematically allowed momentum transfers t. In this procedure, each photon is given a weight $\Delta N_\gamma^{\mathrm{t}}$ according to

$$\Delta N_\gamma^{\mathrm{t}} = \frac{\frac{d\sigma_{\mathrm{em}}}{dt}(s,t)\Delta t}{\sigma_{\mathrm{tot}}(s)}, \tag{4}$$

and the photons are distributed evenly in the azimuthal angle φ. The integral $\sigma_{\mathrm{em}}(s) = \int \frac{d\sigma_{\mathrm{em}}}{dt} dt$ is performed analytically for each channel. The resulting formulas are shown in Appendix E.

Because the width of the ρ-meson is not negligible, its mass distribution has to be taken into account. For the processes with a ρ-meson in the initial state, the actual mass $m_\rho = \sqrt{p_\mu p^\mu}$ of the incoming meson is used for the calculation of the cross section. If there is a ρ-meson in the final state, then first the mass of ρ is chosen randomly according to a Breit-Wigner distribution with mass-dependent width. This mass is then used for all further calculations of this process. Figure 4 shows the cross sections of the channels listed above as a function of $\sqrt{s}$.

B. Photons from hydrodynamics

In the hydrodynamic phase, photons are produced fractionally from every cell on the hydrodynamic grid whose energy density is above a threshold $\varepsilon_{\mathrm{thr}} = 10^{-12}\varepsilon_0$ using the parametrizations by Turbide, Rapp, and Gale [57]. They used an effective nonlinear σ-model Lagrange density in which the vector and axial vector fields are implemented as massive gauge fields of the chiral $U(3)_L \times U(3)_R$ symmetry to obtain the rates. For details on this ansatz, the reader is referred to the original publication [57].

As mentioned earlier, the processes calculated by Turbide *et al.* differ from those considered by Kapusta *et al.* Only the processes $\pi\pi \to \gamma\rho$ and $\pi\rho \to \gamma\pi$ are therefore common to both models. The rate from Turbide *et al.* for $\pi\rho \to \gamma\pi$ directly includes the process with an intermediate a_1-meson.

To simplify the calculations, all photon rates in Ref. [57] are parametrized by the general form

$$E\frac{dR}{d^3p} = A\exp\left[\frac{B}{(2ET)^C} - D\frac{E}{T}\right], \tag{5}$$

where A, B, C, and D are linear functions of some power of the temperature T: $A(T) = A_1 + A_2 T^{A_3}$. The parameter set can be obtained from Ref. [57]. In the rates, the energy E and temperature T are to be given in units of GeV, and the result is given in units of $\mathrm{GeV}^{-2}\,\mathrm{fm}^{-4}$. We also employ the hadronic form factor introduced in Ref. [57].

In the QGP, the rate used is taken from Ref. [58], where the full leading-order result was computed as

$$E\frac{dR}{d^3p} = \sum_{i=1}^{N_f} q_i^2 \frac{\alpha_{\mathrm{em}}\alpha_{\mathrm{S}}}{2\pi^2} T^2 \frac{1}{e^x+1}\left[\ln\left(\frac{\sqrt{3}}{g}\right) + \frac{1}{2}\ln(2x) + C_{22}(x) + C_{\mathrm{brems}}(x) + C_{\mathrm{ann}}(x)\right] \tag{6}$$

and convenient parametrizations were given for the contribution of $2 \leftrightarrow 2$, bremsstrahlung, and annihilation processes (C_{22}, C_{brems}, and C_{ann}, respectively):

$$C_{22}(x) = 0.041x^{-1} - 0.3615 + 1.01\exp(-1.35x), \quad (7a)$$

$$C_{\text{brems}}(x) + C_{\text{ann}}(x) = \sqrt{1+\frac{N_f}{6}}\left[\frac{0.548\ln\left(12.28+\frac{1}{x}\right)}{x^{\frac{3}{2}}} + \frac{0.133x}{\sqrt{1+\frac{x}{16.27}}}\right]. \quad (7b)$$

In Eqs. (6) and (7), $x = E/T$, q_i is the charge of quark flavor i, and α_{em} and $\alpha_S = \frac{g^2}{4\pi}$ are the electromagnetic and QCD coupling constants, respectively. In our calculations, we use $N_f = 3$ and, therefore, $\sum_i q_i^2 = \frac{2}{3}$. The temperature dependence of α_S is taken from Ref. [59] as

$$\alpha_S(T) = \frac{6\pi}{(33-2N_f)\ln\left(\frac{8T}{T_C}\right)}, \quad (8)$$

and the critical temperature at $\mu_B = 0$ is taken to be $T_C = 170$ MeV.

C. Photons from primordial pQCD scatterings

At high transverse momenta, a major contribution to the photon yield is the emission of photons from hard pQCD scatterings of the partons in the incoming protons. In the intermediate- and low-$p_\perp$ regions, the contribution may be comparable to or smaller than the yield from other sources.

We apply the results extracted by Turbide *et al.* [57], who first scaled the photon spectrum from proton-proton collisions by the number of binary collisions in Pb + Pb collisions, and then add a Gaussian-shaped additional $k_\perp$-smearing to the result. The width of the Gaussian is obtained by fitting this procedure to the data from proton-nucleus collisions. The results shown here are obtained with $\langle \Delta k_\perp^2 \rangle = 0.2$ GeV^2.

For comparison, we also show pQCD spectra obtained earlier by Gale [60] following Wong *et al.* [61]. They followed the same procedure as explained earlier. The authors of Ref. [60] obtained a higher intrinsic transverse parton momentum of $\langle \Delta k_\perp^2 \rangle = 0.9$ GeV^2, yet lower spectra.

To compare our calculations to experimental data in Fig. 14, we use the newer calculations by Turbide *et al.* [57].

IV. RATES FROM TRANSPORT AND HYDRODYNAMICS

Before comparing photon spectra from complex nucleus-nucleus collisions between the cascade and hybrid models, we check if both approaches give similar results for the setup of a fully thermalized box.

We perform UrQMD calculations in a box [62], allowing only π-, ρ-, and a_1-mesons to be present and to scatter. When the matter in the box has reached thermal and chemical equilibrium, the rate of photon emission is extracted based on the microscopic scatterings with the procedure described in Sec. III A. Then, we compare the microscopic rates to the hydrodynamic rates from Eq. (5) with the parameters from Ref. [57]. Because the available rates in the cascade and hydrodynamic modes differ, as pointed out earlier, we restrict the comparison to the common rates $\pi\pi \to \gamma\rho$ and $\pi\rho \to \gamma\pi$. The cascade rates are explicitly summed over all charge combinations.

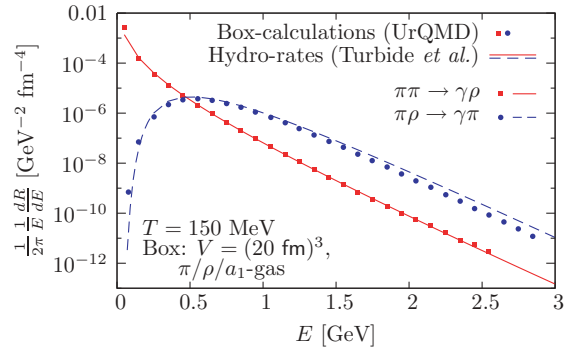

FIG. 5. (Color online) Comparisons between the rates from Ref. [57] (lines) and box calculations restricted to a π, ρ, a_1-system (points) with UrQMD at $T = 150$ MeV.

Figure 5 shows the comparison of the rates at a temperature $T = 150$ MeV. It can be seen that the microscopically obtained rates agree very well with the thermodynamic rates.

V. PHOTON SPECTRA

A. Emission stages

For the present investigation, the evolution of a heavy-ion reaction is divided into three stages: initial stage, intermediate stage, and final stage. The time spans of these stages are defined by the calculations in the hybrid model as before ($t <$ 1.4 fm), during ($1.4 < t < 13.25$ fm for the HG and cascade calculations and $1.4 < t < 30$ fm for the BM calculations), and after the hydrodynamic description ($t > 13.25$ fm, HG and cascade; and $t > 30$ fm, BM). That is, the initial phase denotes the initial string dynamics until the transition to hydrodynamics. Because all differences between the models start at the transition to hydrodynamics, this stage and its contribution is always the same.

Second, the intermediate stage denotes the phase described by hydrodynamics. It starts with the transition to hydrodynamics and ends with the transition back to the cascade. Within this stage, the degrees of freedom may be partonic, hadronic and partonic (in the case of a BM-EOS calculation), or hadronic (in all cases). The final stage starts at the transition from hydrodynamics to the cascade. On average this happens at 13.25 fm for the HG-EOS and 30 fm for the BM-EOS. For pure transport calculations, this phase is also set to start at 13.25 fm, so that a comparison between HG-EOS and cascade calculations is possible. The degrees of freedom in the final stage are hadrons and resonances. The calculations are made with UrQMD in cascade mode and proceed until the last collision has happened.

B. Influence of EOS and dynamics

The contributions of each of these phases to the final spectra are shown in Fig. 6 for the pure cascade calculation and in Fig. 7 for the hybrid calculation with the HG-EOS.

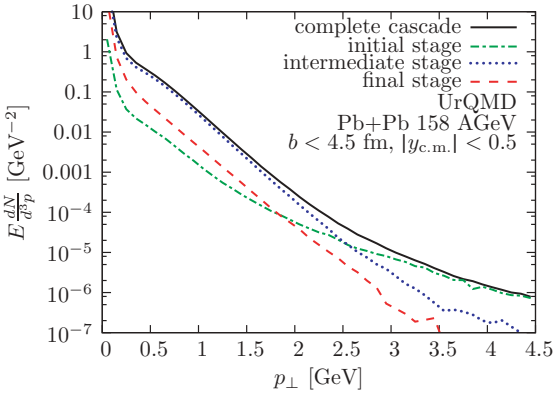

FIG. 6. (Color online) UrQMD calculation. Contributions of the initial [$t < 1.4$ fm, dash-dotted (green) line], intermediate [$1.4 < t < 13.25$ fm, dotted (blue) line], and final [$t > 13.25$ fm, dashed (red) line] stages to the spectrum from pure cascade calculations (solid black line).

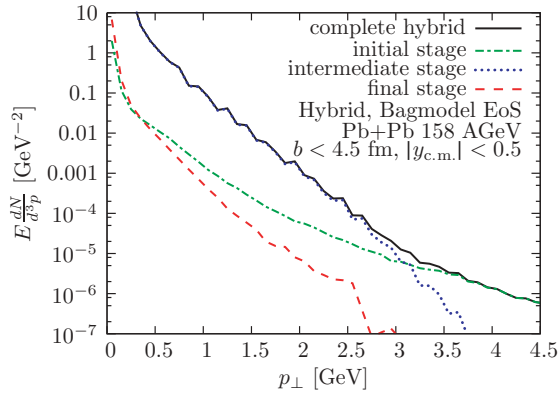

FIG. 8. (Color online) Hybrid model calculation with BM-EOS. Contributions to the initial [(green) dash-dotted line], intermediate [(blue) dotted line], and final [(red) dashed line] stages to the inclusive spectrum (solid black line). In the intermediate stage, the matter is described by hydrodynamics.

In both figures, the black solid lines show the complete direct photon spectra, the (green) dash-dotted lines show the initial-stage contribution, the (red) dashed lines show the photon spectrum from the final phase, and the (blue) dotted lines show the contribution from the intermediate stage. In the hybrid model, the evolution during the intermediate stage is calculated within the hydrodynamic framework. We find that the contribution from this intermediate phase ($1.4 < t < 13.25$ fm) is similar in both models. However, at high transverse momenta $p_\perp > 3$ GeV, the cascade calculation yields more photons from this intermediate time span. This can be related to imperfect thermalization of the system at the transition from the initial nonequilibrium state, which is forced to thermalization at the transition to the hydrodynamic phase but preserved when doing cascade-only calculations. However, Fig. 6 suggests that photon emission toward high transverse momenta from the intermediate stage is in any case strongly suppressed with respect to photon emission from the initial stage. Therefore, neglecting the nonequilibrium effects from the intermediate phase in the hybrid model is justified. The major difference between cascade and hybrid model calculations is the magnitude of the contributions from the final stage [(red) dashed lines]. Here, both models describe the system in the same way. The contribution from this phase to the hybrid-model direct photon spectrum is very similar to the contribution from the intermediate stage. In the pure cascade calculation, however, the final phase contributes roughly a factor of 5 less to the spectrum than the intermediate stage does. A possible explanation is that the transition procedure from hydrodynamic to transport description enhances the number of meson-meson collisions in the late phase.

Interactions at early times ($t < 1.4$ fm) are a significant source of high-transverse-momentum ($p_\perp > 3$ GeV) photons. Here, the thermalized system of the later phase provides only minor contributions to the inclusive spectrum.

In the same analysis that was performed for the hybrid model with the BM-EOS (see Fig. 8), the picture is different. The contribution from the hydrodynamic intermediate stage is strongly enhanced, and the contribution from the final stage after the transition from the hydrodynamic phase is, in turn, reduced with respect to the cases presented before. The total photon spectrum is completely dominated by emission from the hydrodynamic phase at low and intermediate transverse photon momenta ($p_\perp < 3$ GeV). This finding coincides with the observation that the length of the hydrodynamic phase in this model ($\approx$29 fm) is much longer than in the calculations with the HG-EOS ($\approx$12 fm) because of the large latent heat in the setup with the BM-EOS. At high transverse photon momenta, the initial-stage nonequilibrium cascade phase dominates the spectrum, as in the other cases discussed earlier.

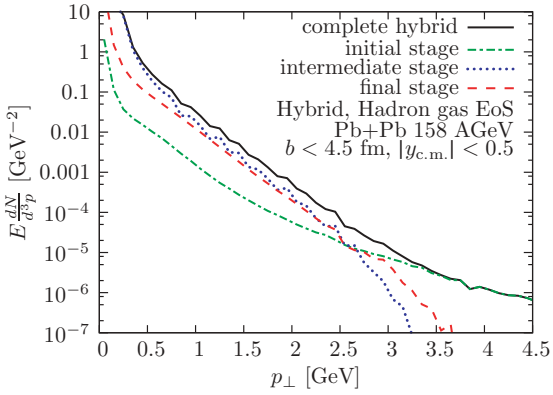

FIG. 7. (Color online) Hybrid model calculation with HG-EOS. Contributions of the initial [dash-dotted (green) line], intermediate [dotted (blue) line], and final [dashed (red) line] stages to the inclusive spectrum (solid black line). In the intermediate stage, the matter is described by hydrodynamics.

C. Channel decomposition

The contributions of the different channels to the hadronic calculations, both in the pure cascade mode and the hybrid approach with a HG-EOS, are shown in Figs. 9 and 10. The

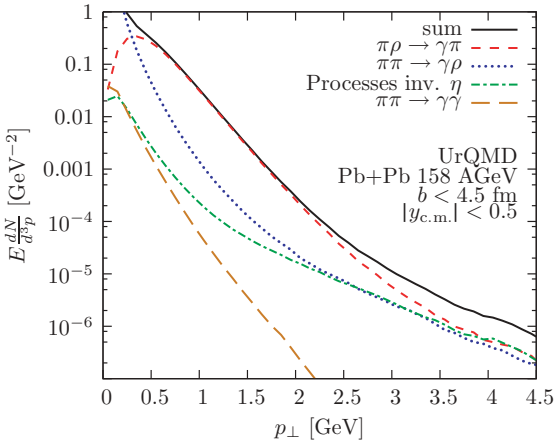

FIG. 9. (Color online) UrQMD calculation. Contributions of the different channels.

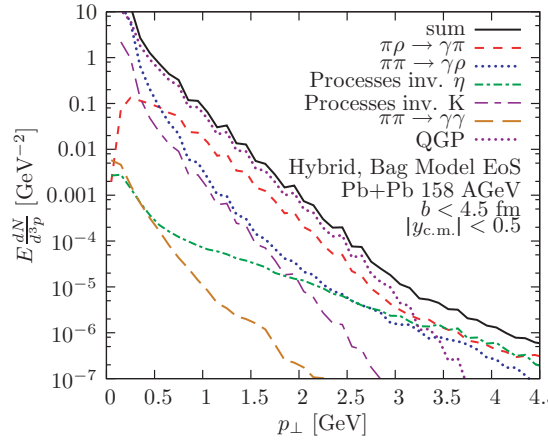

FIG. 11. (Color online) Hybrid-model calculation with BM-EOS. Contributions of the different channels in hybrid calculation with BM-EOS.

dominant contributions in both models are very similar; at low transverse momenta ($p_\perp < 0.5$ GeV), the process with two initial pions $\pi\pi \to \gamma\rho$ is dominant, whereas in the broad range $0.5 < p_\perp < 3.5$ GeV, $\pi\rho \to \gamma\pi$ is the major source of photons. Processes with an η-meson ($\pi\pi \to \gamma\eta$ and $\pi\eta \to \gamma\pi$) become important at high transverse momenta, where they contribute in magnitude similar to the two aforementioned channels. Processes with kaons contribute less to the spectrum than the corresponding nonstrange channels, and the process $\pi\pi \to \gamma\gamma$ is the least significant in all calculations, as expected.

In the photon spectrum extracted from the cascade calculation, one can observe a flattening of the spectrum at high transverse momenta ($p_\perp \approx 3$ GeV). At this point, $\pi\pi \to \gamma\rho$ and η processes start to provide significant contributions to the photon spectrum and lead to a flatter slope already at $p_\perp \approx 2$ GeV. In Sec. VI, we return to this slope change and show it to be consistent with the average emission times of the photons at these transverse momenta.

The calculations with the BM-EOS yield a different picture (see Fig. 11). Here, the dominant contribution comes from the QGP, whose emission magnitude is about two times higher than the combined contribution from all hadronic processes. Again, initial-stage (pre-equilibrium) processes are dominant at high transverse momenta ($p_\perp > 3$ GeV). Apart from that, we observe a similar distribution among the reaction channels as we did earlier (see discussion of Fig. 10); the process $\pi\rho \to \gamma\pi$ is dominant in the intermediate-$p_\perp$ region, $\pi\pi \to \gamma\rho$ dominates the hadronic contribution at low $p_\perp$, and the early scatterings in those channels and the channels involving η-mesons contribute to the high-$p_\perp$ region in approximately equal amounts.

Figure 12 shows a comparison of hybrid-model calculations with HG-EOS and transport calculations, using only common channels applied to a dynamic system (see Fig. 5 for a static comparison). One observes that the direct photon spectrum is not sensitive to the change in the underlying dynamics (e.g., finite viscosities vs ideal fluid), which indicates that even the two-body collision dynamic in UrQMD drives the system into equilibrium in the π-ρ-a_1 channel.

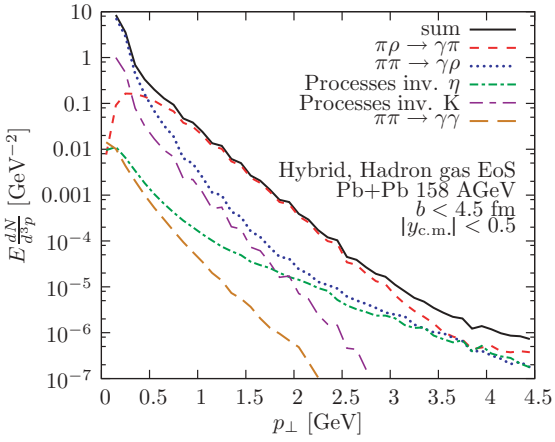

FIG. 10. (Color online) Hybrid-model calculation with HG-EOS. Contributions of the different channels.

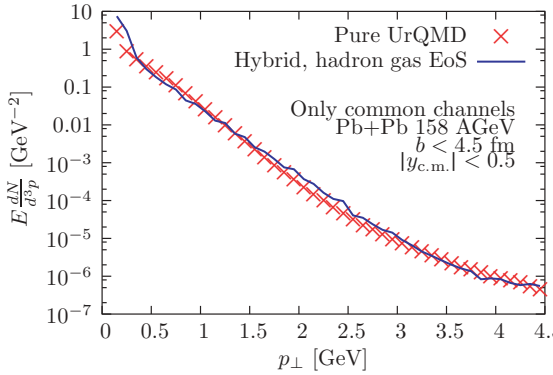

FIG. 12. (Color online) Comparison of direct photon spectra from the hybrid model with HG-EOS and transport model, using only common channels.

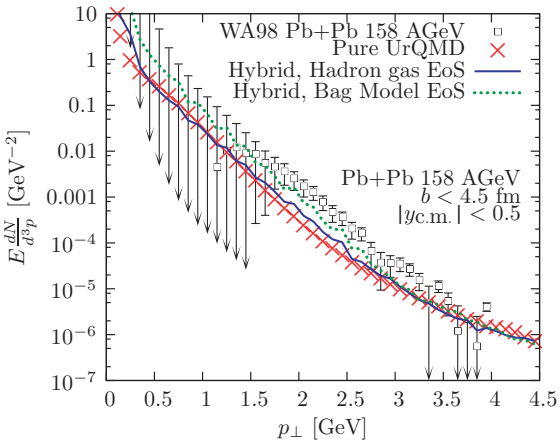

FIG. 13. (Color online) Comparison of the direct photon spectra from all variations of the model to the experimental data of the WA98 Collaboration [8]. Calculations without intermediate hydrodynamic stage (pure cascade mode) are shown as (red) crosses, hybrid calculations with HG-EOS as a (blue) solid line, and BM calculations as the (dark green) dotted line. The data contain no photons from initial proton-proton collisions.

D. Comparison to data

A comprehensive comparison between the models presented above and experimental data is shown in Fig. 13. Here, we show the sum over all channels and all stages in the cases of pure UrQMD calculations and hybrid models with HG- and BM-EOS. The BM-EOS yields the highest photon spectra and provides a reasonable description of the data from the WA98 Collaboration [8]. The purely hadronic calculations, with and without intermediate hydrodynamic calculation, give smaller yields than the scenario with a QGP.

After adding the pQCD spectra as extracted in Ref. [57], we obtain Fig. 14. Because of the rather large pQCD contribution, the difference between the spectra with varying EOS is reduced, and all calculations agree very well with the data.

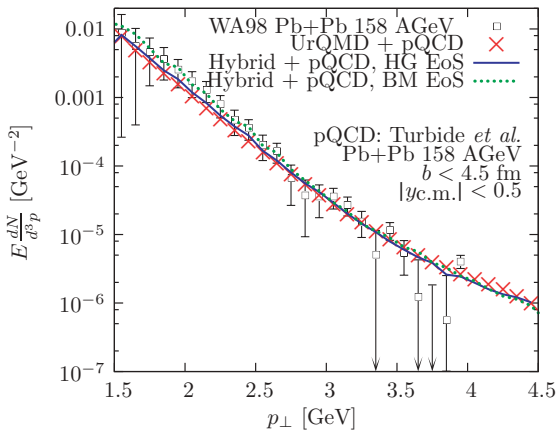

FIG. 14. (Color online) Comparison of the direct photon spectra from the model, with added pQCD photons from Ref. [57], to the experimental data by the WA98 Collaboration [8]. Calculations without intermediate hydrodynamic stage (pure cascade mode) are shown as (red) crosses, hybrid calculations with HG-EOS as a (blue) solid line, and BM calculations as a (dark green) dotted line.

VI. SENSITIVITY TO DIFFERENT EMISSION TIMES AND PROCESSES

To investigate the major sources of photons for the transverse momentum spectrum and to explore the sensitivity to the different reaction stages, we investigate the origin of the change of slope of the spectra at high transverse momenta $p_\perp \approx 3$ GeV in Figs. 15, 16, and 17 within UrQMD. Two processes may contribute to high-$p_\perp$ photons: (i) collisions with a large $\sqrt{s}$ in elementary reactions (i.e., early stage collisions) and (ii) collisions of particles with large transverse flow $q_\perp$ but rather small $\sqrt{s}$ (i.e., late-stage collisions). To disentangle these effects, we determine the contributions of scatterings with high center-of-mass energy $\sqrt{s} > 4$ GeV and high center-of-mass transverse momentum $q_\perp > 3$ GeV. Figure 15 shows the transverse-momentum spectrum of photons split up into the two contributions. Nearly all photons at high transverse momenta (shaded gray area) come from collisions with high center-of-mass energies, whereas the contribution of high center-of-mass transverse momenta only shows a trivial structure at $p_\perp \approx q_\perp^{\text{threshold}} = 3$ GeV.

One cross-check for Fig. 15 is shown in Fig. 16. Here, the collision spectrum is exponential. Only at high transverse boosts can a deviation from an exponential spectrum be seen. This indicates that most photons with high transverse momentum come from unboosted collisions with $q_\perp < 1$ GeV. The center-of-mass energy and transverse momentum of a collision show no correlation.

The latter can be seen in Fig. 17, where the photon production rate is shown as a function of the center-of-mass energy of the individual collisions. The figure confirms the notion that most photons with high transverse momenta come from collisions with high center-of-mass energies. However, it is worthwhile to observe that, starting at $\sqrt{s_{\text{coll}}} = 7$ GeV,

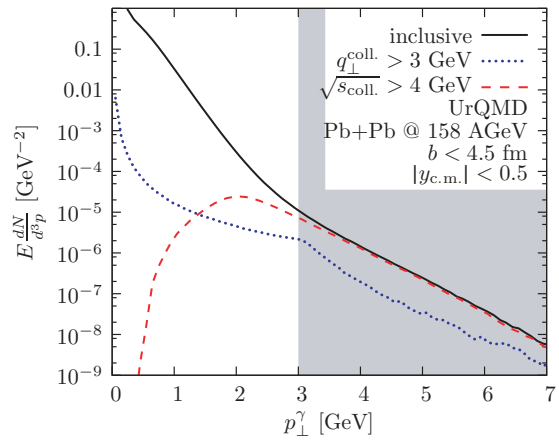

FIG. 15. (Color online) UrQMD calculation. The $p_\perp$ spectra for all photons (solid black line), photons from boosted collisions [dotted (blue) line], and collisions with high center-of-mass energy [dashed (red) line]. The shaded gray area indicates the range of the $p_\perp$ region used for the solid black lines in Figs. 16 and 17.

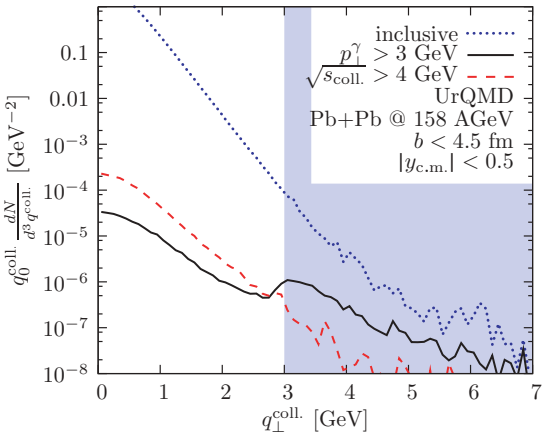

FIG. 16. (Color online) UrQMD calculation. The number of photons as a function of the transverse center-of-mass momentum of the elementary collision, $q^{\rm coll}$: all photons [(blue) dotted line], photons that have high transverse momentum (black solid line), and photons from collisions with high center-of-mass energy [(red) dashed line]. The (light blue) shaded area indicates the range of the $q_\perp$ region used for the dotted (blue) lines in Figs. 15 and 17.

each elementary collision produces essentially only photons with transverse momenta $p_\perp > 3$ GeV. The distribution of center-of-mass energies also shows that the vast majority of collisions happen around the ρ- and a_1-pole masses.

Figure 18 shows the average emission times of photons as a function of the transverse momentum for the various channels. It is noticeable that, over a very broad momentum range ($0.3 < p_\perp < 2.1$ GeV), the average emission time stays at a constant level of about $\langle t_{\rm emission}\rangle \approx 8$ fm. This coincides with the region where the process $\pi\rho \to \gamma\pi$ dominates. Only at high transverse momenta do the early times dominate. This is consistent with the findings in Sec. V in which the spectrum

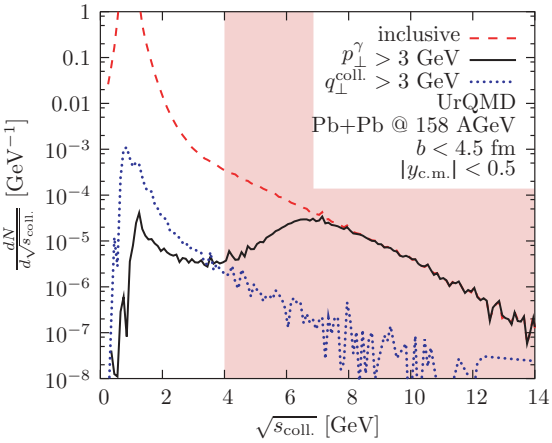

FIG. 17. (Color online) UrQMD calculation. The number of photons as a function of the center-of-mass energy of the elementary collision: all photons [(red) dashed line], photons that have high transverse momentum (black solid line), and photons from collisions with high transverse center-of-mass momentum. The (light red) shaded area shows the range of the $\sqrt{s}$ region used for the (red) dashed lines in Figs. 15 and 16.

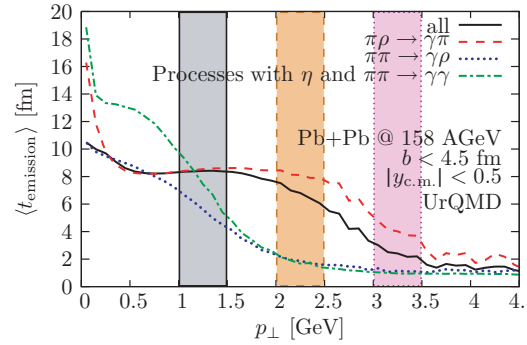

FIG. 18. (Color online) UrQMD calculation. Average photon emission times as a function of the transverse momentum for all photons, $\pi\rho \to \gamma\pi$, $\pi\pi \to \gamma\rho$, and other processes [black solid, (red) dashed, (blue) dotted, and (green) dash-dotted lines, respectively]. The shaded areas correspond to the $p_\perp$ regions used for the curves shown in Fig. 19.

clearly shows two different temperatures, one in the region below $p_\perp = 2.5$ GeV and a different temperature above $p_\perp > 3$ GeV. It also explains why the spectral contributions from $\pi\pi \to \gamma\rho$ and η processes show a much flatter slope already at $p_\perp \approx 2$ GeV. At late times, when the average center-of-mass energy has decreased, photons are predominantly produced at low transverse momenta.

Figure 19 shows the emission time distribution of photons in various $p_\perp$ bins for the $\pi\rho \to \gamma\pi$ processes. It is interesting to see that, at all transverse momenta, there is an initial flash of photons emitted at very early times ($t \approx 1$ fm). In the low-$p_\perp$ bin, $1 < p_\perp < 1.5$ GeV, a very strong contribution from the bulk emission in the hot-and-dense stage between $t = 4$ fm and $t = 12$ fm raises the average emission time. In the intermediate-$p_\perp$ region ($2 < p_\perp < 2.5$ GeV), the bulk contribution is greatly reduced and shines less brightly than the initial flash. In the highest-$p_\perp$ region ($3 < p_\perp < 3.5$ GeV), the late bulk contribution is small and the initial stage dominates.

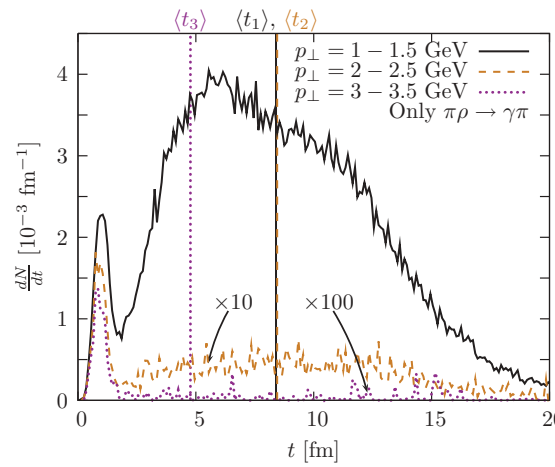

FIG. 19. (Color online) UrQMD calculation. Emission time distribution of photons from $\pi\rho$ scatterings for the different photon transverse-momentum regions indicated in Fig. 18. The vertical lines indicate the average emission time in the corresponding $p_\perp$ bin.

However, one should note that, because of the long lifetime of the intermediate stage, the average emission times are shifted to higher values.

VII. SUMMARY

In this work, we studied direct photon emission from hadronic and partonic sources within three different dynamical models. In Sec. III, we presented a model for photon emission from microscopic collisions (Sec. III A) and from thermal rates (Sec. III B). Then, we introduced the cross sections and thermal rates used for the present calculations.

In Sec. IV, we showed that the emission rates from a thermalized microscopic cascade calculation agree very well with the thermal rates used in the hydrodynamic part of the present model. We discussed the contributions from the different stages before, during, and after the high-density part of the evolution to the direct photon spectra for cascade calculations as well as HG and BM hybrid calculations. It was found that the relative contributions of photons in the hybrid calculation with HG-EOS and cascade simulations are similar. In contrast, in the BM calculations, the intermediate high-density hydrodynamic phase takes a much longer time and contributes substantially more to the photon spectra.

Investigations that differentiate between the different channels showed that the process $\pi\rho \to \gamma\pi$ is the dominant hadronic source for photon production at intermediate photon transverse momenta ($0.5 < p_\perp < 3$ GeV), while $\pi\pi \to \gamma\rho$ is dominant at low photon transverse momenta ($p_\perp < 0.5$ GeV) only.

When comparing the different variations of the model (see Fig. 13), we found that both the hybrid model and the cascade model can explain the spectra measured by the WA98 Collaboration [8], if pQCD photons are included. By comparison of Figs. 12 and 13, we can also conclude that the photon yields from the hybrid-model calculation with HG-EOS and the pure transport calculation are equal within uncertainties, if the same sets of channels are used in the calculations.

We also found that photons at high transverse momenta ($p_\perp > 3$ GeV) show a significantly flatter slope (and therefore higher effective temperature) than photons with lower $p_\perp$. This effect was attributed to higher center-of-mass energies that produce these photons, and we found that it is not significantly influenced by elementary collisions that have a high center-of-mass boost in the transverse direction. The analysis of average photon emission times showed that photons at $p_\perp > 3$ GeV are emitted significantly earlier than at lower transverse momenta.

We also discussed different model assumptions (see Appendixes A and B), namely photon emission from colliding string ends, and compared those to pQCD spectra. The result indicated that direct photon emission from string ends is restricted to the early phase of the collision where the medium is hot. Neglecting those collisions lowers the effective temperature at high transverse momenta ($p_\perp > 2.5$ GeV). In any case, string-end contributions can be neglected in comparison with the pQCD contribution.

We found that the inclusion of a finite width of the produced ρ-mesons is relevant only at low transverse momenta. That is, the effect of assigning the pole mass or a mass chosen randomly according to the spectral function is important only in the lowest $p_\perp$ bin.

VIII. OUTLOOK

The good agreement between the calculations presented here and the experimental data shows that the cascade plus hydrodynamic hybrid model provides an excellent tool to explore the properties of QCD matter at energies where the (onset of) deconfinement is expected. We plan to extend the investigation to a more realistic EOS with chiral restoration, critical end point, and rapid crossover [63]. Also, the decays of short-lived mesons and baryons, which cannot be subtracted by the experiment, may play a major role in enhancing the direct photon spectra and will therefore be investigated.

Furthermore, direct photon emission will be investigated for the systems studied or planned to be studied at the RHIC (PHENIX), the Large Hadron Collider (ALICE), Facility for Antiproton and Ion Research (CBM), and Schwerionensynchrotron-100 (HADES).

More differential observables like direct photon elliptic flow can also be explored in the present model.

ACKNOWLEDGMENTS

This work was supported by the Frankfurt Center for Scientific Computing, the GSI, and the BMBF. The authors thank Hannah Petersen for providing the hybrid and Dirk Rischke for the hydrodynamic code, as well as Jan Steinheimer-Froschauer for the equation of state. B. Bäuchle gratefully acknowledges support from the Deutsche Telekom Stiftung and the Helmholtz Research School on Quark Matter Studies. This work was supported by the Hessian LOEWE initiative through the Helmholtz International Center for FAIR. The authors thank Elvira Santini and Pasi Huovinen for valuable discussions and Klaus Reygers for experimental clarifications.

APPENDIX A: DISCUSSION OF STRING ENDS

In UrQMD, the leading particles from a string have a reduced cross section during their formation time. For all other purposes, they are treated as hadrons. (Hadronic) Scatterings of the string ends happen typically at high center-of-mass energies $\sqrt{s}$. Collisions from string ends can only produce photons if the collision of fully formed hadrons of the same type would produce photons. Thus, their contribution is treated as an addition to the prompt contribution from primordial nucleus-nucleus interactions. Photons from those collisions contribute significantly to the spectra at high transverse momenta. Because these particles are not fully formed hadrons, but effectively represent quarks or diquarks, a hadronic treatment of those processes is questionable.

The effects of including the photons from colliding string ends, that is, the interaction of leading (di)quarks, in the calculation can be seen in Fig. 20. The spectrum obtained by

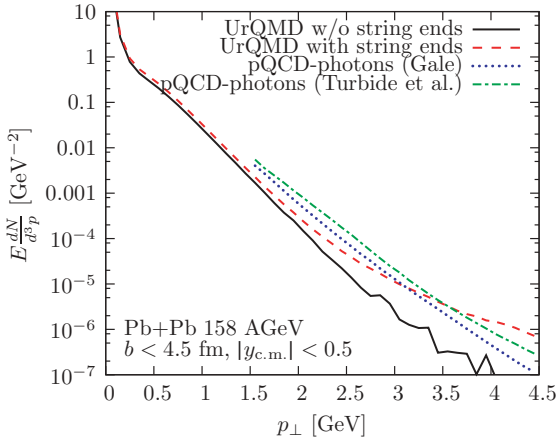

FIG. 20. (Color online) UrQMD calculation. Total yields of photons with (dashed line) and without (solid line) the contributions from colliding string ends.

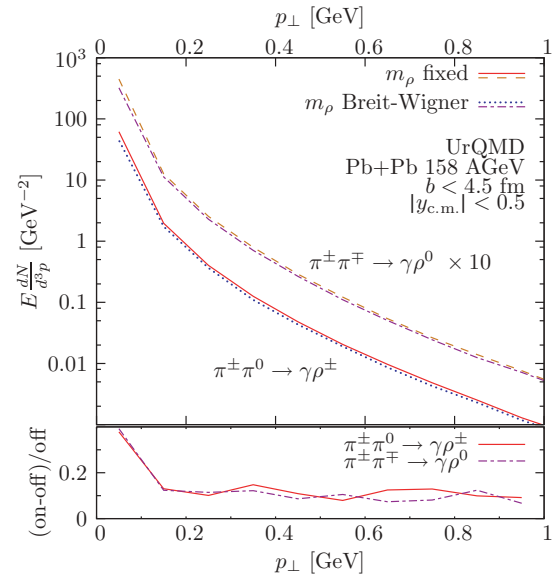

FIG. 21. (Color online) UrQMD calculation. Photon spectra from collisions that produce a ρ-meson in the final state for the production of ρ-mesons at its pole mass (solid and dashed lines) and for the production of ρ-mesons according to a Breit-Wigner mass distribution (dotted and dash-dotted lines).

neglecting the collision of string ends is exponential and does not exhibit the flattening at high transverse photon momenta. The inclusion of (di)quark scatterings, however, leads to a strong increase of the photon yield at high $p_\perp$. The contribution of pQCD photons to the inclusive spectrum already begins to be significant at relatively low transverse photon momenta ($p_\perp \approx 1$ GeV), although the magnitude of the contribution differs between the different parametrizations in Refs. [57] and [60].

APPENDIX B: DISCUSSION OF ρ-MESON WIDTH

Earlier we discussed the handling of the ρ-meson's finite width. Figure 21 shows the effects of following the calculation outlined there. In both channels, $\pi^\pm\pi^\mp \to \gamma\rho^0$ and $\pi^\pm\pi^0 \to \gamma\rho^\pm$, the yield is about 10% higher for ρ's produced at their pole mass, and only at very low momenta does this excess become as large as 40%.

This behavior can be explained by kinematic arguments: By far the highest scattering rate in $\pi + \pi$ collisions is at $\sqrt{s} \approx m_\rho^0$. Here, the photon cross section with fixed pole mass is much higher than the extended calculation with variable ρ mass. At all other center-of-mass energies, the extended model gives a higher cross section, but these comparatively rare processes provide only a minor contribution to the spectrum. The processes at low $\sqrt{s}$ contribute primarily to the low-$p_\perp$ region, because the production of the ρ-meson consumes most of the available energy. Therefore, the enhancement in the model is most pronounced at low $p_\perp$.

APPENDIX C: COMPARISON TO OLDER WORKS WITH UrQMD

As mentioned in Sec. II, UrQMD was used previously to obtain direct photon spectra [46]. The authors calculated transverse-momentum spectra for central ($b = 0$ fm) Pb + Pb collisions at $E_{\rm lab} = 160A$ GeV. Limiting ourselves to the same conditions, we can compare our work to that of Dumitru *et al.* In Fig. 22, we compare results from the current UrQMD version 2.3 to those obtained with the earlier versions, 1.3 (using our own photon analysis) and 1.0 (taken from Ref. [46]). The older UrQMD versions yield significantly higher photon spectra at intermediate $p_\perp$.

We can identify two changes in UrQMD that lead to this behavior. Between versions 1.0 (used by Dumitru *et al.*) and 1.3, the angular distributions of various processes were improved. Because the collisions of pions with a high difference in rapidity provide significant contributions to the spectra from Ref. [46], the improved angular distributions reduce the photon production cross section. Furthermore, in versions prior to 2.3, the number of pions has been unphysically high. The correction of this leads to fewer collisions involving pions and, hence, to a further reduction of the spectra.

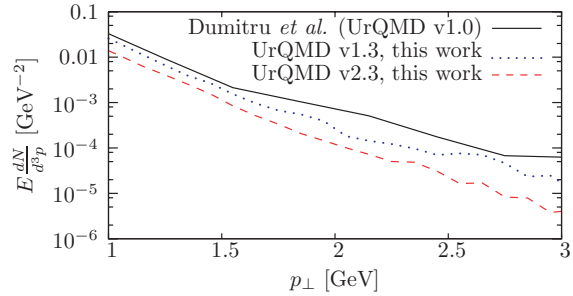

FIG. 22. (Color online) Comparison of the current model [(red) dashed line] to calculations from Dumitru *et al.* (Ref. [46], black solid line). For further comparision, we apply our model to an earlier UrQMD version [(blue) dotted line].

APPENDIX D: DIFFERENTIAL CROSS SECTIONS

For completeness, we list the differential cross sections for the processes used in [11,12].

$$\frac{d\sigma}{dt}(\pi^{\pm}\pi^{\mp}\to\gamma\rho^0)=\frac{\alpha g_\rho^2}{4sp_{\text{c.m.}}^2}\left\{2-\left(m_\rho^2-4m_\pi^2\right)\left[\frac{s-2m_\pi^2}{s-m_\rho^2}\frac{1}{t-m_\pi^2}+\frac{m_\pi^2}{\left(t-m_\pi^2\right)^2}+(t\leftrightarrow u)\right]\right\}, \tag{D1a}$$

$$\frac{d\sigma}{dt}(\pi^{\pm}\pi^0\to\gamma\rho^{\pm})=-\frac{\alpha g_\rho^2}{16sp_{\text{c.m.}}^2}\left[\frac{\left(s-2m_\rho^2\right)\left(t-m_\pi^2\right)^2}{m_\rho^2\left(s-m_\rho^2\right)^2}+\frac{\left(s-6m_\rho^2\right)\left(t-m_\pi^2\right)}{m_\rho^2\left(s-m_\rho^2\right)}+\frac{4s\left(m_\rho^2-4m_\pi^2\right)}{\left(s-m_\rho^2\right)^2}\right.$$
$$\left.+\frac{4\left(m_\rho^2-4m_\pi^2\right)}{t-m_\pi^2}\left(\frac{s}{s-m_\rho^2}+\frac{m_\pi^2}{t-m_\pi^2}\right)+\frac{m_\pi^2}{m_\rho^2}-\frac{9}{2}+(t\leftrightarrow u)\right], \tag{D1b}$$

$$\frac{d\sigma}{dt}(\pi^{\pm}\rho^0\to\gamma\pi^{\pm})=\frac{\alpha g_\rho^2}{12sp_{\text{c.m.}}^2}\left\{2-\frac{s\left(m_\rho^2-4m_\pi^2\right)}{\left(s-m_\pi^2\right)^2}-\frac{\left(m_\rho^2-4m_\pi^2\right)}{t-m_\pi^2}\left[\frac{s-m_\rho^2+m_\pi^2}{\left(s-m_\pi^2\right)\left(t-m_\pi^2\right)}+\frac{m_\pi^2}{\left(t-m_\pi^2\right)}\right]\right\}, \tag{D1c}$$

$$\frac{d\sigma}{dt}(\pi^{\pm}\rho^{\mp}\to\gamma\pi^0)=-\frac{\alpha g_\rho^2}{48sp_{\text{c.m.}}^2}\left\{4\left(m_\rho^2-4m_\pi^2\right)\left[\frac{t}{\left(t-m_\pi^2\right)^2}+\frac{u}{\left(u-m_\rho^2\right)^2}-\frac{m_\rho^2}{s-m_\pi^2}\left(\frac{1}{t-m_\pi^2}+\frac{1}{u-m_\rho^2}\right)\right]\right.$$
$$\left.+\left(3+\frac{s-m_\pi^2}{m_\rho^2}\right)\frac{s-m_\pi^2}{u-m_\rho^2}-\frac{1}{2}+\frac{s}{m_\rho^2}-\left(\frac{s-m_\pi^2}{u-m_\rho^2}\right)^2\right\}, \tag{D1d}$$

$$\frac{d\sigma}{dt}(\pi^0\rho^{\pm}\to\gamma\pi^{\pm})=\frac{\alpha g_\rho^2}{48sp_{\text{c.m.}}^2}\left\{\frac{9}{2}-\frac{s}{m_\rho^2}-\frac{4s\left(m_\rho^2-4m_\pi^2\right)}{\left(s-m_\pi^2\right)^2}+\frac{\left(s-m_\pi^2\right)^2-4m_\rho^2\left(m_\rho^2-4m_\pi^2\right)}{\left(u-m_\rho^2\right)^2}\right.$$
$$\left.+\frac{1}{u-m_\rho^2}\left[5\left(s-m_\pi^2\right)-\frac{\left(s-m_\pi^2\right)^2}{m_\rho^2}-\frac{4\left(m_\rho^2-4m_\pi^2\right)\left(s-m_\pi^2+m_\rho^2\right)}{s-m_\pi^2}\right]\right\}, \tag{D1e}$$

$$\frac{d\sigma}{dt}(\pi^{\pm}\pi^{\mp}\to\gamma\eta)=\frac{\pi\alpha A|F_\pi(s)|^2}{16m_\eta^2m_\rho^4sp_{\text{c.m.}}^2}\left[s\left(u-m_\pi^2\right)\left(t-m_\pi^2\right)-m_\pi^2\left(s-m_\eta^2\right)^2\right], \tag{D1f}$$

$$\frac{d\sigma}{dt}(\pi^{\pm}\eta\to\gamma\pi^{\pm})=\frac{\pi\alpha A|F_\pi(u)|^2}{16m_\eta^2m_\rho^4sp_{\text{c.m.}}^2}\left[u\left(s-m_\pi^2\right)\left(t-m_\pi^2\right)-m_\pi^2\left(u-m_\eta^2\right)^2\right], \tag{D1g}$$

$$\frac{d\sigma}{dt}(\pi^{\pm}\pi^{\mp}\to\gamma\gamma)=\frac{2\pi\alpha^2}{sp_{\text{c.m.}}^2}\left[1+2m_\pi^2\left(\frac{1}{t-m_\pi^2}+\frac{1}{u-m_\pi^2}\right)+2m_\pi^4\left(\frac{1}{t-m_\pi^2}+\frac{1}{u-m_\pi^2}\right)^2\right]. \tag{D1h}$$

In these equations, $t=(p_\pi-p_\gamma)^2$ is always the momentum transfer from the pion to the photon[1] (unlike the convention used in Ref. [11]) and $p_{\text{c.m.}}=(2\sqrt{s})^{-1}\sqrt{s^2-2s(m_1^2+m_2^2)+(m_1^2-m_2^2)^2}$ is the three-momentum of the incoming particles in the center-of-mass frame (m_1 and m_2 being their masses). The value of A is, consistent with Ref. [11], $A=g_{\eta\rho\rho}^2g_\rho^2/4\pi\gamma_\rho^2=4.7$, and the pion electromagnetic form factor is

$$F_\pi(s)=\frac{m_\rho^4}{\left(s-m_\rho^2\right)+\Gamma_\rho^2m_\rho^2}.$$

In their 1992 paper, Xiong *et al.* [12] calculated the cross section for the formation of an intermediate a_1-meson during $\pi\rho$ scattering, averaged over all possible charge combinations:

$$\frac{d\sigma}{dt}(\pi\rho\to a_1\to\gamma\pi)=\frac{\pi^2\sqrt{s}}{2p_{\text{c.m.}}^3(s-m_\pi)^2}\frac{\Gamma_{a_1\to\pi\rho}\Gamma_{a_1\to\gamma\pi}}{(\sqrt{s}-m_{a_1})^2+(\Gamma_{a_1\to\pi\rho}+\Gamma_{a_1\to\gamma\pi})^2/4}. \tag{D1i}$$

This channel is not included in Ref. [11]. Xiong *et al.* obtained this from a Lagrange density involving only the pion, photon, ρ-, and a_1-fields:

$$\mathcal{L}=G_\rho a_1^\mu[g_{\mu\nu}(p_\pi p_\rho)-p_{\pi\mu}p_{\rho_\nu}]\rho^\nu\Phi+G_\rho\frac{e}{g_\rho}a_1^\mu[g_{\mu\nu}(p_\pi p_\gamma)-p_{\pi\mu}p_{\gamma\nu}]A^\nu\Phi, \tag{D2}$$

[1] All cases with two pions in the initial state are symmetric in $t\leftrightarrow u$. Therefore, it is not necessary to specify which pion is the reference for t.

where $G_\rho = 14.8\,\mathrm{GeV}^{-1}$. The partial widths of the a_1, $\Gamma_{a_1\to\pi\rho}$ and $\Gamma_{a_1\to\gamma\pi}$, are estimated to be

$$\Gamma_{a_1\to\pi\rho} = \frac{G_\rho^2 p_{\mathrm{c.m.}}}{24\pi m_{a_1}^2}\left\{\frac{m_\rho^2}{4s}\left[s-\left(m_\rho^2-m_\pi^2\right)\right] + \frac{1}{2}\left(s-m_\rho^2-m_\pi^2\right)\right\} \tag{D3a}$$

$$\Gamma_{a_1\to\gamma\pi} = \frac{G_\rho^2\alpha p_{\mathrm{c.m.}}}{12 g_\rho^2 m_{a_1}^2}\left(s-m_\pi^2\right). \tag{D3b}$$

APPENDIX E: INTEGRATED CROSS SECTIONS

The integration over the cross sections listed in Appendix D yield the following results:

$$\sigma(\pi^\pm\pi^\mp\to\gamma\rho^0) = \frac{\alpha g_\rho^2}{4sp_{\mathrm{c.m.}}^2}\left\{2\Delta t-\left(m_\rho^2-4m_\pi^2\right)\left[\frac{s-2m_\pi^2}{s-m_\rho^2}\ln\frac{\left(t_- - m_\pi^2\right)}{\left(t_+ - m_\pi^2\right)}+\frac{m_\pi^2\Delta t}{\left(m_\pi^2-t_+\right)\left(m_\pi^2-t_-\right)}+\left(t_\pm\leftrightarrow u_\mp\right)\right]\right\}, \tag{E1a}$$

$$\sigma(\pi^\pm\pi^0\to\gamma\rho^\pm) = -\frac{\alpha g_\rho^2}{16sp_{\mathrm{c.m.}}^2}\left\{\frac{s-2m_\rho^2}{m_\rho^2\left(s-m_\rho^2\right)^2}\frac{1}{3}\left(t_-^3-t_+^3\right)+\frac{s-6m_\rho^2}{m_\rho^2\left(s-m_\rho^2\right)}\frac{1}{2}\left(t_-^2-t_+^2\right)+\left[\frac{4s\left(m_\rho^2-4m_\pi^2\right)}{\left(s-m_\rho^2\right)^2}+\frac{m_\pi^2}{m_\rho^2}-\frac{9}{2}\right]\right.$$
$$\left.\Delta t+\frac{4s\left(m_\rho^2-4m_\pi^2\right)}{\left(s-m_\rho^2\right)}\ln\frac{t_- - m_\pi^2}{t_+ - m_\pi^2}+\frac{4m_\pi^2\left(m_\rho^2-4m_\pi^2\right)\Delta t}{\left(m_\pi^2-t_+\right)\left(m_\pi^2-t_-\right)}+\left(t_\pm\leftrightarrow u_\mp\right)\right\}, \tag{E1b}$$

$$\sigma(\pi^\pm\rho^0\to\gamma\pi^\pm) = \frac{\alpha g_\rho^2}{12sp_{\mathrm{c.m.}}^2}\left\{2\Delta t-\frac{s\left(m_\rho^2-4m_\pi^2\right)}{\left(s-m_\pi^2\right)^2}\Delta t-\left(m_\rho^2-4m_\pi^2\right)\left[\frac{s-m_\rho^2+m_\pi^2}{s-m_\pi^2}\ln\frac{t_- - m_\pi^2}{t_+ - m_\pi^2}+\frac{m_\pi^2\Delta t}{\left(m_\pi^2-t_+\right)\left(m_\pi^2-t_-\right)}\right]\right\}, \tag{E1c}$$

$$\sigma(\pi^\pm\rho^\mp\to\gamma\pi^0) = -\frac{\alpha g_\rho^2}{48sp_{\mathrm{c.m.}}^2}\left\{4\left(m_\rho^2-4m_\pi^2\right)\left[\frac{m_\pi^2\Delta t}{\left(u_+ - m_\rho^2\right)\left(u_- - m_\rho^2\right)}+\frac{m_\pi^2\Delta t}{\left(t_+ - m_\pi^2\right)\left(t_- - m_\pi^2\right)}\right.\right.$$
$$+\ln\frac{u_+ - m_\rho^2}{u_- - m_\rho^2}+\ln\frac{t_- - m_\pi^2}{t_+ - m_\pi^2}-\frac{m_\rho^2}{s-m_\pi^2}\left(\ln\frac{t_- - m_\pi^2}{t_+ - m_\pi^2}+\ln\frac{u_+ - m_\rho^2}{u_- - m_\rho^2}\right)\Bigg]$$
$$\left.+\left(s-m_\pi^2\right)\left(3+\frac{s-m_\pi^2}{m_\rho^2}\right)\ln\frac{u_+ - m_\rho^2}{u_- - m_\rho^2}+\Delta t\left[\frac{s}{m_\rho^2}-\frac{1}{2}-\frac{\left(s-m_\pi^2\right)^2}{\left(u_+ - m_\rho^2\right)\left(u_- - m_\rho^2\right)}\right]\right\}, \tag{E1d}$$

$$\sigma(\pi^0\rho^\pm\to\gamma\pi^\pm) = \frac{\alpha g_\rho^2}{48sp_{\mathrm{c.m.}}^2}\left\{\Delta t\left[\frac{9}{2}-\frac{s}{m_\rho^2}-\frac{4s\left(m_\rho^2-4m_\pi^2\right)}{\left(s-m_\pi^2\right)^2}+\frac{\left(s-m_\pi^2\right)^2-4m_\rho^2\left(m_\rho^2-4m_\pi^2\right)}{\left(u_+ - m_\rho^2\right)\left(u_- - m_\rho^2\right)}\right]\right.$$
$$\left.+\left[5\left(s-m_\pi^2\right)-\frac{\left(s-m_\pi^2\right)^2}{m_\rho^2}-\frac{4\left(m_\rho^2-4m_\pi^2\right)\left(s-m_\pi^2+m_\rho^2\right)}{s-m_\pi^2}\right]\ln\frac{u_+ - m_\rho^2}{u_- - m_\rho^2}\right\}, \tag{E1e}$$

$$\sigma(\pi^\pm\pi^\mp\to\gamma\eta) = \frac{\pi\alpha A|F_\pi(s)|^2}{16m_\eta^2 m_\rho^4 sp_{\mathrm{c.m.}}^2}\left\{\left(2m_\pi^2+m_\eta^2-s\right)\frac{s}{2}\left(t_+^2-t_-^2\right)-\frac{s}{3}\left(t_+^3-t_-^3\right)-m_\pi^2\left[m_\eta^4+s\left(m_\pi^2-m_\eta^2\right)\right]\right\}, \tag{E1f}$$

$$\sigma(\pi^\pm\eta\to\gamma\pi^\pm) = \frac{\pi\alpha A}{16m_\eta^2 sp_{\mathrm{c.m.}}^2}\left\{-m_\pi^2\left[\left(t_- + u_-\right)\left(s-m_\pi^2\right)+\left(2m_\pi^2-s\right)^2\right]I_0\right.$$
$$+\left[\left(s-m_\pi^2\right)\left(m_\pi^2+t_- + u_-\right)-2m_\pi^2\left(s-2m_\pi^2\right)\right]\left[\left(t_- + u_- - m_\rho^2\right)I_0+\frac{1}{2}I_1\right]$$
$$\left.-s\left[\Delta t+\left(t_- + u_- - m_\rho^2\right)I_1+\left(t_- + u_- - m_\rho^2\right)^2 I_0 - m_\rho^2\Gamma_\rho^2 I_0\right]\right\}, \tag{E1g}$$

$$\sigma(\pi^\pm\pi^\mp\to\gamma\gamma) = \frac{2\pi\alpha^2}{sp_{\mathrm{c.m.}}^2}\left\{\Delta t+2m_\pi^2\left[\left(1-\frac{2m_\pi^2}{s}\right)\ln\frac{t_- - m_\pi^2}{t_+ - m_\pi^2}+\frac{m_\pi^2\Delta t}{\left(t_- - m_\pi^2\right)\left(t_+ - m_\pi^2\right)}+\left(t_\pm\leftrightarrow u_\mp\right)\right]\right\}, \tag{E1h}$$

$$\sigma(\pi\rho\to a_1\to\gamma\pi) = 4p_1\omega\frac{d\sigma}{dt}(\pi\rho\to a_1\to\gamma\pi). \tag{E1i}$$

In those equations, $t_\pm = m_1^2 - 2\omega(E_1 \pm p_1)$ are the minimal and maximal allowed momentum transfers, and correspondingly $u_\pm = m_1^2 + m_2^2 + m_4^2 - s - t_\pm$, and Δt is shorthand for $t_- - t_+$. The indices 1, 2, and 4 denote the particles in the order given on the left-hand side of the equations (3 is the photon). E_1, p_1, and $\omega = E_3$ denote momentum and energy of the respective particles in the center-of-mass frame. In the cross section $\pi^\pm\eta \to \gamma\pi^\pm$ [Eq. (E1g)], the following notations have been used for simplicity:

$$I_0 = \frac{1}{m_\rho \Gamma_\rho}\left[\arctan\left(\frac{u_+ - m_\rho^2}{m_\rho\Gamma_\rho}\right) - \arctan\left(\frac{u_- - m_\rho^2}{m_\rho\Gamma_\rho}\right)\right] \tag{E2a}$$

$$I_1 = \ln\left[\frac{\left(u_- - m_\rho^2\right)^2 + m_\rho^2\Gamma_\rho^2}{\left(u_+ - m_\rho^2\right)^2 + m_\rho^2\Gamma_\rho^2}\right]. \tag{E2b}$$

[1] J. W. Harris and B. Muller, Annu. Rev. Nucl. Part. Sci. **46**, 71 (1996).
[2] S. A. Bass, M. Gyulassy, H. Stoecker, and W. Greiner, J. Phys. G **25**, R1 (1999).
[3] J. Adams *et al.* (STAR Collaboration), Nucl. Phys. A **757**, 102 (2005).
[4] B. B. Back *et al.*, Nucl. Phys. A **757**, 28 (2005).
[5] I. Arsene *et al.* (BRAHMS Collaboration), Nucl. Phys. A **757**, 1 (2005).
[6] K. Adcox *et al.* (PHENIX Collaboration), Nucl. Phys. A **757**, 184 (2005).
[7] C. Alt *et al.* (NA49 Collaboration), Phys. Rev. C **77**, 024903 (2008).
[8] M. M. Aggarwal *et al.* (WA98 Collaboration), arXiv:nucl-ex/0006007.
[9] S. S. Adler *et al.* (PHENIX Collaboration), Phys. Rev. Lett. **94**, 232301 (2005).
[10] A. Adare *et al.* (PHENIX Collaboration), arXiv:0804.4168 [nucl-ex].
[11] J. I. Kapusta, P. Lichard, and D. Seibert, Phys. Rev. D **44**, 2774 (1991); **47**, 4171(E) (1993).
[12] L. Xiong, E. V. Shuryak, and G. E. Brown, Phys. Rev. D **46**, 3798 (1992).
[13] K. Geiger, Comput. Phys. Commun. **104**, 70 (1997).
[14] S. A. Bass *et al.*, Prog. Part. Nucl. Phys. **41**, 255 (1998).
[15] M. Bleicher *et al.*, J. Phys. G **25**, 1859 (1999).
[16] W. Ehehalt and W. Cassing, arXiv:hep-ph/9507274.
[17] D. Molnar and P. Huovinen, Phys. Rev. Lett. **94**, 012302 (2005).
[18] Z. Xu and C. Greiner, Phys. Rev. C **71**, 064901 (2005).
[19] Z. W. Lin, C. M. Ko, B. A. Li, B. Zhang, and S. Pal, Phys. Rev. C **72**, 064901 (2005).
[20] G. Burau, J. Bleibel, C. Fuchs, A. Faessler, L. V. Bravina, and E. E. Zabrodin, Phys. Rev. C **71**, 054905 (2005).
[21] S. A. Bass, T. Renk, and D. K. Srivastava, Nucl. Phys. A **783**, 367 (2007).
[22] H. W. Barz and B. Kampfer, Nucl. Phys. A **683**, 594 (2001).
[23] W. Cassing, Nucl. Phys. A **700**, 618 (2002).
[24] A. B. Larionov, O. Buss, K. Gallmeister, and U. Mosel, Phys. Rev. C **76**, 044909 (2007).
[25] J. Bleibel, G. Burau, A. Faessler, and C. Fuchs, Phys. Rev. C **76**, 024912 (2007).
[26] J. Bleibel, G. Burau, and C. Fuchs, Phys. Lett. B **659**, 520 (2008).
[27] J. Cleymans and K. Redlich, *Lattice QCD and the Hydrodynamic Expansion of the Quark-Gluon Plasma* (Bielefeld U.), BI-TP 85/35, Dec. 1985, 13pp.
[28] M. Kataja, P. V. Ruuskanen, L. D. McLerran, and H. von Gersdorff, Phys. Rev. D **34**, 2755 (1986).
[29] H. Von Gersdorff, L. McLerran, M. Kataja, and P. V. Ruuskanen, Phys. Rev. D **34**, 794 (1986).
[30] M. Kataja, Z. Phys. C **38**, 419 (1988).
[31] D. K. Srivastava and B. Sinha, Phys. Lett. B **261**, 1 (1991).
[32] D. K. Srivastava, B. Sinha, and T. C. Awes, Phys. Lett. B **387**, 21 (1996).
[33] D. K. Srivastava, B. Sinha, M. Gyulassy, and X. N. Wang, Phys. Lett. B **276**, 285 (1992).
[34] D. K. Srivastava, J. Alam, S. Chakrabarty, S. Raha, and B. Sinha, Phys. Lett. B **278**, 225 (1992).
[35] J. Cleymans and H. Satz, Z. Phys. C **57**, 135 (1993).
[36] D. H. Rischke, Y. Pursun, and J. A. Maruhn, Nucl. Phys. A **595**, 383 (1995); **596**, 717(E) (1996).
[37] T. Hirano, Phys. Rev. C **65**, 011901(R) (2001).
[38] P. Huovinen, P. V. Ruuskanen, and S. S. Rasanen, Phys. Lett. B **535**, 109 (2002).
[39] P. Huovinen, M. Belkacem, P. J. Ellis, and J. I. Kapusta, Phys. Rev. C **66**, 014903 (2002).
[40] P. F. Kolb and U. W. Heinz, arXiv:nucl-th/0305084.
[41] C. Nonaka and S. A. Bass, Phys. Rev. C **75**, 014902 (2007).
[42] E. Frodermann, R. Chatterjee, and U. Heinz, J. Phys. G **34**, 2249 (2007).
[43] K. Dusling and D. Teaney, Phys. Rev. C **77**, 034905 (2008).
[44] R. Baier, P. Romatschke, and U. A. Wiedemann, Phys. Rev. C **73**, 064903 (2006).
[45] H. Song and U. W. Heinz, Phys. Rev. C **78**, 024902 (2008).
[46] A. Dumitru, M. Bleicher, S. A. Bass, C. Spieles, L. Neise, H. Stöcker, and W. Greiner, Phys. Rev. C **57**, 3271 (1998).
[47] D. K. Srivastava and K. Geiger, Phys. Rev. C **58**, 1734 (1998).
[48] E. L. Bratkovskaya, S. M. Kiselev, and G. B. Sharkov, Phys. Rev. C **78**, 034905 (2008).
[49] H. Petersen, M. Bleicher, S. A. Bass, and H. Stocker, arXiv:0805.0567 [hep-ph].
[50] T. Sjostrand, S. Mrenna, and P. Z. Skands, J. High Energy Phys. 05 (2006) 026.
[51] H. Petersen, J. Steinheimer, G. Burau, M. Bleicher, and H. Stocker, Phys. Rev. C **78**, 044901 (2008).
[52] J. Steinheimer, M. Mitrovski, T. Schuster, H. Petersen, M. Bleicher, and H. Stoecker, Phys. Lett. B **676**, 126 (2009).
[53] H. Petersen, M. Mitrovski, T. Schuster, and M. Bleicher, Phys. Rev. C **80**, 054910 (2009).
[54] Q. f. Li, J. Steinheimer, H. Petersen, M. Bleicher, and H. Stocker, Phys. Lett. B **674**, 111 (2009).
[55] H. Petersen, J. Steinheimer, M. Bleicher, and H. Stocker, J. Phys. G **36**, 055104 (2009).

[56] H. Petersen, J. Steinheimer, G. Burau, and M. Bleicher, Eur. Phys. J. C **62**, 31 (2009).
[57] S. Turbide, R. Rapp, and C. Gale, Phys. Rev. C **69**, 014903 (2004).
[58] P. B. Arnold, G. D. Moore, and L. G. Yaffe, J. High Energy Phys. 12 (2001) 009.
[59] F. M. Liu and K. Werner, J. Phys. G **36**, 035101 (2009).
[60] C. Gale, Nucl. Phys. A **698**, 143 (2002).
[61] C. Y. Wong and H. Wang, Phys. Rev. C **58**, 376 (1998).
[62] M. Belkacem *et al.*, Phys. Rev. C **58**, 1727 (1998).
[63] J. Steinheimer, V. Dexheimer, H. Petersen, M. Bleicher, S. Schramm, and H. Stoecker, arXiv:0905.3099 [hep-ph].